ACS APPLIED MATERIALS & INTERFACES

Research Article

www.acsami.org

A Simple Descriptor to Rapidly Screen CO Oxidation Activity on Rare-Earth Metal-Doped CeO_2: From Experiment to First-Principles

Kyeounghak Kim,[†,∥] Jeong Do Yoo,[‡,∥] Siwon Lee,[‡] Minseok Bae,[§] Joongmyeon Bae,[§] WooChul Jung,*[,‡] and Jeong Woo Han*[,†]

[†]Department of Chemical Engineering, University of Seoul, Seoul 02504, Republic of Korea

[‡]Department of Materials Science and Engineering and [§]Department of Mechanical Engineering, Korea Advanced Institute of Science and Technology, Daejeon 34141, Republic of Korea

Supporting Information

ABSTRACT: Ceria (CeO_2) is an attractive catalyst because of its unique properties, such as facile redoxability and high stability. Thus, many researchers have examined a wide range of catalytic reactions on ceria nanoparticles (NPs). Among those contributions are the reports of the dopant-dependent catalytic activity of ceria. On the other hand, there have been few mechanistic studies of the effects of a range of dopants on the chemical reactivity of ceria NPs. In this study, we examined the catalytic activities of pure and Pr, Nd, and Sm-doped CeO_2 (PDC, NDC, and SDC, respectively) NPs on carbon monoxide (CO) oxidation. Density functional theory (DFT) calculations were also performed to elucidate the reaction mechanism on rare-earth (RE)-doped CeO_2(111). The experimental results showed that the catalytic activities of CO oxidation were in the order of CeO_2 > PDC > NDC > SDC. This is consistent with the DFT results, where the reaction is explained by the Mars-van Krevelen mechanism. On the basis of the theoretical interpretation of the experimental results, the ionic radius of the RE dopant can be used as a simple descriptor to predict the energy barrier at the rate-determining step, thereby predicting the entire reaction activity. Using the descriptor, a wide range of RE dopants on CeO_2(111) were screened for CO oxidation. These results provide useful insights to unravel the CO oxidation activity on various oxide catalysts.

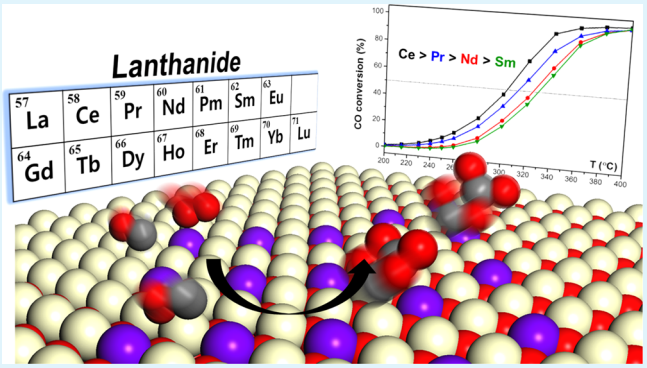

KEYWORDS: *CO oxidation, rare-earth, doping, ceria, oxide catalyst, density functional theory*

1. INTRODUCTION

Ceria (CeO_2) has been intensively studied in the field of heterogeneous catalysis with a variety of applications, such as automotive emission control, catalytic combustion, hydrocarbon reforming, and electrocatalytic reactions.[1−9] The remarkable features of ceria make it a suitable catalyst, including the intriguing ability of facile redox between Ce^{4+}/Ce^{3+}, high oxygen storage capacity (OSC) coupled with the formation of oxygen vacancies, and exceptional stability over a wide range of temperatures and gas atmospheres.[9]

Despite the extensive research on CeO_2-based catalysts, most focused on tailoring the nanoscale architectures of ceria to improve its chemical reactivity. Previous studies have shown that the catalytic properties of ceria can be tuned by changing its size, shape, and/or morphology, particularly when it is on the nanoscale.[10−16] On the other hand, few studies have examined the influence of dopants on the chemical reactivity of ceria nanoparticles (NPs). With the exception of Cu, which facilitates the rate of carbon monoxide (CO) oxidation,[17,18] many transition metals (TMs) and noble metals are unsuitable as a choice of dopant because of their limited solubility in the ceria host lattice and/or thermal stability.[19−22] In contrast, ceria can accommodate a wide range of rare-earth (RE) elements. For example, when doped with trivalent elements, such as Sm or Gd, ceria is used widely as a promising solid electrolyte with excellent oxygen ion conductivity at intermediate temperatures (400−600 °C).[23−25] The introduction of tetravalent elements (e.g., Zr^{4+} and Hf^{4+}) enhances the OSC and thermal stability.[8,26]

Only a few studies have reported the dopant-dependent chemical reactivity of RE-doped ceria nanocatalysts, whose conclusions still remain controversial. Reddy's group[27−30] examined the catalytic activity toward CO oxidation with a series of RE dopants, in which the reactivity was in the following order, Hf > Sm > Eu > Gd > Ce > La > Pr > Zr. Prasad et al.[31] and Harshini et al.[32] investigated the impact of dopants (Y, La, Pr, Sm, Eu, Gd, Tb, and Yb) on the Ce−Zr−RE and Ce−Hf−RE systems for CO and soot oxidation,

Received: February 7, 2017
Accepted: April 18, 2017
Published: April 18, 2017

DOI: 10.1021/acsami.7b01844
ACS Appl. Mater. Interfaces 2017, 9, 15449−15458

respectively, and reported that in contrast to Reddy's results, Pr was most active and even better than Sm. In contrast to the abovementioned reports, Gorte's group reported the detrimental effects of acceptor dopants (Y, La, Sm, Gd, and Yb) on propane and *n*-butane oxidation.[33,34] This inconsistency between different experiments comes partly from the fact that most studies used ill-defined particle structures in terms of the size and specific surface area, which may strongly affect the catalytic performance of ceria NPs. Therefore, it is essential to carry out reliable and quantitative experiments to clearly distinguish the chemical effect of the dopant from the particle's geometric one.

Computational approaches have played an important role in elucidating the CO oxidation mechanism on ceria-based catalysts and providing a promising dopant element.[35−42] Most studies, however, focused on the TMs and noble metals, such as Mn,[42] Ru,[41] Fe,[40] Pd,[43] and Zr,[44] as dopant candidates for $CeO_2(111)$, showing that the TM or noble metal dopants facilitate the formation of surface oxygen vacancies, which may promote CO oxidation. Recently, the Mars-van Krevelen (MvK) mechanism has been used widely to describe the oxidation reactions on metal oxide catalysts. Kim et al. applied the mechanism to explain CO oxidation at the interface between the Au nanocluster and pure[45] or X-doped $CeO_2(111)$ (X = Au, Pt, Ti, Ru, and Zr),[37] demonstrating that doped CeO_2 can be a good support material to accelerate CO oxidation.

In this contribution, to understand the true effects of RE dopants on the CO oxidation activity upon CeO_2 catalysis and resolve the previous controversy, ceria particles were synthesized with similar geometries with a varying choice of RE dopants, followed by the quantitative reactivity tests in combination with DFT analysis for elucidating the reaction mechanism. A series of $Ce_{0.8}RE_{0.2}O_{2-\delta}$ (RE = Pr, Sm, and Nd) and undoped ceria NPs were carefully synthesized, using an ethylenediamenetetraacetate (EDTA)−citrate complexing method,[46] to keep the size and surface area of ceria particles constant regardless of the dopant type. The physical and chemical attributes of each catalyst were characterized using a broad range of analytical tools, such as thermogravimetric analysis (TGA), X-ray diffraction (XRD), transmission electron microscopy (TEM), Brunauer−Emmett−Teller (BET) surface area measurements, and inductively coupled plasma-mass spectrometry (ICP-MS). The catalytic reactivity of RE-doped CeO_2 was tested for the CO oxidation reaction in a fixed-bed reactor with a gas mixture of CO and O_2 in Ar. In addition, DFT calculations were used to describe the reaction mechanism via MvK, and a key descriptor on molecular adsorption and desorption to rapidly predict the oxidation activity of RE-doped $CeO_2(111)$ was found.

2. METHODS

2.1. Catalyst Preparation. $Ce_{0.8}RE_{0.2}O_{2-\delta}$ (RE = Ce, Pr, Sm, and Nd) NPs with a diameter of 12.8 ± 0.1 nm were synthesized by an EDTA−citrate complexing method.[46] Figure S8 describes the overall synthetic process in this study. Stoichiometric amounts of nitrate-based, cation precursors were dissolved in deionized water, and a mixture of EDTA and citric acid, serving as a chelating agent and fuel for combustion, was added. Subsequently, the pH values of the mixed solution were adjusted in the range of 4−10, using $NH_3{\cdot}H_2O$. The EDTA/citric acid/total cation ion molar ratios were fixed at 1:2:1. The solution was then evaporated on a hot-plate at 80 °C and then heated further to 260 °C to form a crispy solid precursor. The combustion of the solid precursor was conducted in a heating mantle at 450 °C for 1 h, followed by calcination in a box furnace at 750 °C for 3 h.

2.2. Characterization Techniques. The temperature-dependent weight losses of the predried precursors were measured by TGA (TGA 92-18; Setaram) at a heating rate of 7 °C/min in air (Figure S9). XRD (D/MAX 2500; Rigaku) with Cu Kα radiation (λ = 1.5418 Å) at 40 kV and 200 mA at a scan rate of 4 °C/min from 25 to 90° was used to identify the crystal structures and extract the crystallite sizes and lattice parameters of the ceria powders. The elemental compositions of the powders were analyzed by ICP-MS (7700S IPC-MS; Agilent). BET measurements (Quantachrom, Autosorb-1, N_2 at 77.3 K) were conducted to evaluate the specific surface area. The powder morphologies were examined further by TEM (Philips Tecnai F20, JEOL JEM-3010).

2.3. Catalytic Tests. All of the experiments were conducted at atmospheric pressure in a fixed-bed flow quartz reactor. To build a catalytic bed, 100 mg of the catalyst mixed with 200 mg of the silica beads was loaded between 30 mg of the silica beads for each side. For CO oxidation, the reactant gas mixture consisted of 0.5 vol % CO, 20 vol % O_2, and 79.5 vol % Ar and was fed at 40 mL min^{-1}. The reactant and product gases were monitored using a quadrupole mass spectrometer (GSD320; PFEIFFER Vacuum) in real time. The conversion ratio was detected by the m/e = 44 peak (the major peak of CO_2) instead of the 28 peak (the major peak of CO) to avoid interference caused by the fragmented CO_2 (m/e = 28, 11.4%). Gas chromatography (6890N; Agilent) was also used to calibrate the gas compositions precisely.

2.4. Computational Details. To analyze the mechanism of CO oxidation on RE metal-doped CeO_2, density functional theory (DFT) calculations were performed using the Vienna ab initio simulation package.[47,48] A (2 × 2) surface unit cell of $CeO_2(111)$ with a vacuum thickness of 16 Å was used (Figure S10). The (111) surface is the most stable among the low Miller index surfaces[35,36,49,50] and shows the largest fraction of surface exposure on the polycrystalline ceria powders.[51] Theoretically, the (100) surface of CeO_2 is the most active toward CO oxidation; and thus, many studies have been conducted using the cube-shaped ceria particles, which are presumed to be mainly exposed to the (100) surface. However, since these particles are not stable at high temperatures, they are not suitable for the studies which require high temperatures, as in this study. Moreover, the actual surfaces of shape-controlled particles are known to exhibit a much higher degree of nonuniformity at the atomistic level than generally expected. For example, Wang and Woll et al. recently demonstrated that rod-shaped ceria NPs, which had been previously assumed to expose a (110)-terminated surface, undergo extensive restructuring, and consequently, {111}-type faceting becomes an intrinsic property of the ceria(110) surface.[52] Therefore, $CeO_2(111)$ has been the best representative of the catalyst phenomena used in many applications, showing good agreement with the experimental results.[40−42]

The exchange-correlation energies were treated using the Perdew−Burke−Ernzerhof functional on the basis of a generalized gradient approximation (GGA).[53] A plane wave expansion, with a cutoff of 400 eV, was used with a 2 × 2 × 1 Monkhorst−Pack k-point[54] sampling of the Brillouin zone. Gaussian smearing was used with a width of 0.1 eV to determine the partial occupancies. The geometries were relaxed using a conjugate gradient algorithm until the forces on all unconstrained atoms were less than 0.03 eV/Å. To take the on-site Coulomb and exchange interaction of localized electrons into account, the GGA + U scheme, with the effective U value of 5.0, was used to describe the localized nature of the 4f electrons of Ce.[37,45] The details for calculating the energetics are described comprehensively in the Supporting Information.

3. RESULTS AND DISCUSSION

3.1. Physical and Chemical Characterization of Ceria Particles. To clearly investigate the dopant-dependent catalytic properties of ceria NPs, it is important to eliminate their morphological complexities. In this regard, ceria particles with a similar size and surface area were synthesized, but only with different types of dopants. The pH of the precursor solution had a strong effect on the crystallite size of the samples (Figure

DOI: 10.1021/acsami.7b01844
ACS Appl. Mater. Interfaces 2017, 9, 15449−15458

S1), which is related directly to the specific surface area and possibly catalytic activity. In this sense, different pH values need to be set depending on the dopant to secure a well-defined particle structure between samples.

XRD of the RE-doped CeO_2 samples used in this study showed that all samples have a cubic fluorite structure without secondary phases (Figure S2). Furthermore, according to the Scherrer equation, the mean crystallite sizes of all of the samples were also estimated, confirming that they are similar (12.8 ± 0.1 nm) to each other. Figure 1 presents TEM images

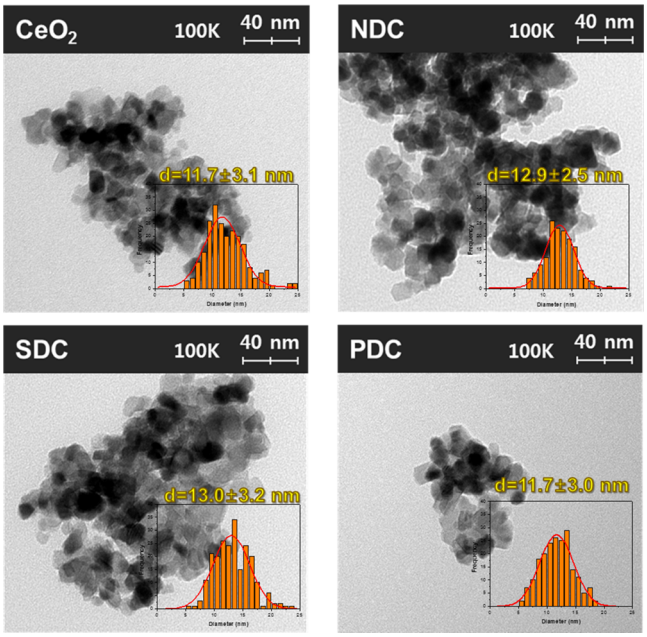

Figure 1. TEM images and particle size distributions of doped ceria NPs.

of ceria particles. The histograms of the size distribution are presented (insert), which were obtained by counting 200 particles for each sample. The mean particle sizes obtained from the image analysis were in the range of 11.7−12.9 nm, which concur with the values from XRD. The particles in this study did not show any specific shapes with a preferred terminated surface. In fact, cube and rhombic dodecahedron particles, which are the most stable in the {100} and {110} surfaces, respectively, were not noticeably observed and the shape of the ceria particles used was almost constant regardless of the type of dopant. Instead, the ideal morphology of CeO_2 derived from the Wulff construction typically exhibits an octahedral shape exposing the {111} facets.[55,56] Therefore, this study assumes that the {111} surface, which is known to be the most thermodynamically stable,[51,57] is dominant in our ceria powders and performs the related DFT calculations. Additional BET measurements were also undertaken to compare the specific surface area of each particle. All samples maintained similar specific surface areas in the range of 46.1−56.7 m^2/g. The corresponding particle sizes, on the basis of the assumption of an ideal spherical shape, were calculated to be between 14.7 and 18.3 nm, which are slightly larger, but still similar to the values from both XRD and TEM. Table 1 lists the geometric information of the synthesized ceria particles.

Furthermore, the chemical compositions of all samples were also analyzed by ICP-MS, which showed that the RE dopant concentrations of all samples were approximately 20% within

Table 1. Doping Concentration (RE), Lattice Constant, XRD Crystallite Size (D_{XRD}), TEM Particle Size (D_{TEM}), BET Particle Size (D_{BET}), and BET Surface Area (S_{BET}) of Doped Ceria NPs

sample	RE[a] (mol %)	lattice constant[b] (Å)	D_{XRD} (nm)	D_{BET} (nm)	S_{BET} (m^2/g)	D_{TEM} (nm)
CeO_2		5.4135	12.9	14.7	56.7	11.7
NDC	19.8 ± 0.1	5.4554	12.6	17.7	48.4	12.9
PDC	19.7 ± 0.1	5.4192	12.7	16.5	50.5	11.7
SDC	19.8 ± 0.1	5.4430	12.8	18.3	46.1	13.0
average			12.8	16.8	50.4	12.3
standard deviation			0.1	1.4	4.0	0.6

[a]From ICP-MS, the errors were determined by measuring three times for each sample. [b]From XRD analysis.

an error of only 0.1%. Overall, the particles obtained in this study show highly controlled morphologies and compositions. Consequently, they serve as an appropriate model system to quantitatively analyze the effects of the dopants on the catalytic properties of ceria NPs.

3.2. CO Oxidation Reactivity of Doped Ceria NPs. The catalytic properties of doped ceria NPs were tested for the CO oxidation reaction in the temperature range of 150−480 °C. Figure 2a shows the typical CO conversion ratio as a function of the reaction temperature over the four samples, with different dopants. Figure 2a also presents the CO conversion behaviors without ceria catalysts for comparison. As an indicator of the reactivity for CO oxidation, the T_{50} value (corresponding temperature at 50% conversion of CO to CO_2) was used. Pure CeO_2 showed the highest activity for CO oxidation with the lowest T_{50} value, whereas it was suppressed when RE was added. The corresponding T_{50} values for CeO_2, PDC, NDC, and SDC were 304, 312, 324, and 328 °C, respectively. Given that the standard deviation in T_{50} of ceria NPs, which were calculated from four different measurements, was within ±1.5 °C (see Figure S3), the catalytic activities of doped ceria NPs increase in the following order: CeO_2 > PDC > NDC > SDC. Interestingly, as the atomic number of the dopants increased and the ionic radius decreased, the ceria catalysts became more active toward the CO oxidation reaction.

The kinetic rate data revealed a difference in the intrinsic activity among the catalysts used in this work. To observe the intrinsic surface kinetics, the point was set below the 12% conversion ratio region. As shown in Figure 2b, pure CeO_2 exhibited a 4.3 times higher reaction rate at 240 °C compared to that of SDC. More importantly, the apparent activation energies of the ceria NPs tended to increase with increasing T_{50} value. For example, the activation energy of the pure CeO_2 NP, that is the most reactive one, was 83.8 kJ/mol, whereas the least reactive SDC showed a value of 103.9 kJ/mol. This correlation between the dopant and apparent activation energy will be discussed further in detail.

3.3. Theoretical Interpretation of CO Oxidation on Doped CeO_2(111): MvK Mechanism. MvK mechanism has been widely used to explain CO oxidation reaction on bare and doped CeO_2 surfaces.[35,37,38] The experimental results were interpreted on the basis of the mechanism. To examine the detailed oxidation process on RE-doped CeO_2(111), the relative reaction energy profile via the MvK mechanism was plotted, as shown in Figure 3, which is on the basis of the energetic state of each elementary step labeled E0 to E5 and IS1 to IS2, respectively. Here, the reaction energy, which is the

DOI: 10.1021/acsami.7b01844
ACS Appl. Mater. Interfaces 2017, 9, 15449−15458

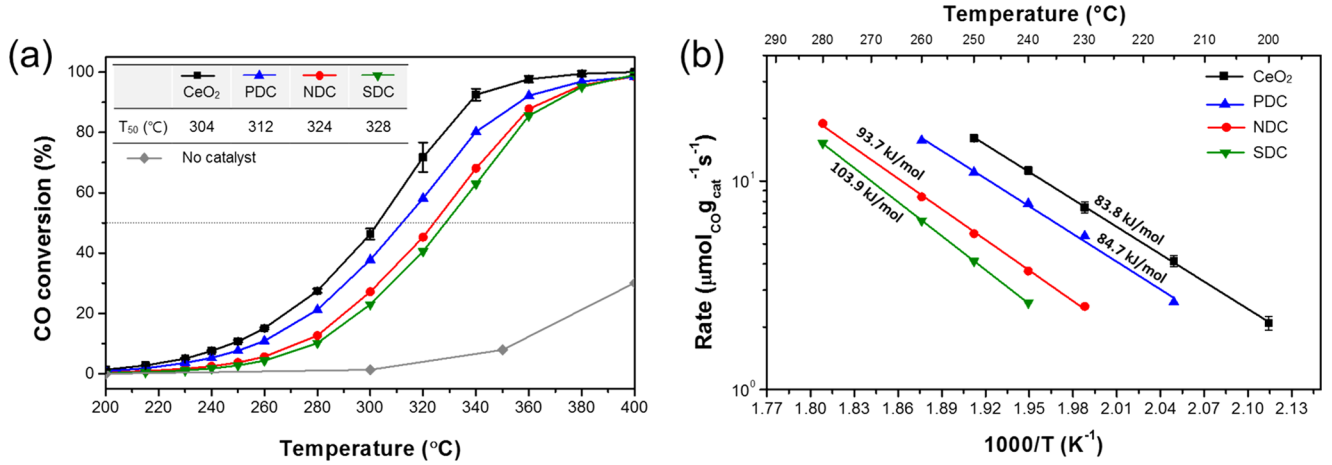

Figure 2. (a) Light-off plots for CO oxidation over doped ceria NPs. (b) Arrhenius plots for CO oxidation over doped ceria NPs. The activation energies are indicated above each line.

energy difference between the initial and final states, is believed to describe the energy barrier between the reaction steps under the assumption of a Brønsted–Evans–Polanyi (BEP) relationship. The BEP model is an efficient way to estimate the activation energy (E_b) from the reaction energy on $CeO_2(111)$.[58] To confirm that the BEP relationship is valid in this system, climbing image-nudged elastic band calculations[59] were performed to estimate the rigorous reaction barriers between E4 and IS2 (barrier 3), as an example (Figure S4). E_b showed a linear relationship with the reaction energy, implying that the BEP relationship holds for the step between E4 and IS2 (Figure S5). Therefore, it is reasonably presumed that the reaction energies at the other elementary steps in Figure 3 can also successfully predict the reaction barriers; thus, it is possible to determine the rate-determining step (RDS) by comparing the reaction energies of each elementary step.

Although the conventional MvK mechanism[35,39] has not often considered the adsorbed carbonate species during the CO oxidation process, two additional carbonate formation steps should be included in the reaction mechanism to obtain the precise reaction barriers on doped[40−42] or nondoped $CeO_2(111)$.[38] Using DFT + U calculations, Chen et al. showed that the CO that exists as carbonate species on pure $CeO_2(111)$ is 0.1 eV more stable than that of adsorbed CO_2 at the first oxidation process[38] (in this study, E0 to E1 in Figure 3). This is because the orbital hybridization of the surface Ce 4f and O 2p orbitals with the 2p orbital of CO_2 stabilizes the adsorbed CO_2 on the surface by forming a carbonate species with significant charge transfer from carbonate to $CeO_2(111)$.[38,60] Chen et al. calculated the frequencies of molecular adsorption to demonstrate that carbonite (CO^{2-}) and carbonate (CO_3^{2-}) species could be formed during the oxidation reaction on M-doped $CeO_2(111)$ (M = Mn, Ru, and Fe).[40−42] In particular, the formation of surface carbonate species was calculated to be more stable than that of CO_2 species adsorbed on Fe-doped CeO_2.[40] Recently, Xie et al. explored the CO adsorption and desorption on Sm-doped $CeO_2(111)$ using DFT calculations. In their study, Sm-doped $CeO_2(111)$ had a lower E_{vf} than pure $CeO_2(111)$, which may enhance CO oxidation due to the modified geometric and electronic structure of Sm-doped $CeO_2(111)$.[61] On the other hand, their results are contradictory to the current experimental and theoretical results. One main difference from the present study is that they did not consider carbonate formation during the oxidation process.

Carbonate-like (CO_3^{2-}) species has also been observed experimentally during the oxidation reaction on doped CeO_2. Wu et al. examined CO oxidation over various surface planes, such as rods ({110} + {111}), cubes ({100}), and octahedra ({111}). Their IR spectra showed that a variety of carbonate species are formed by the strong interaction between the surface oxygen and CO molecules at room temperature.[11] These theoretical and experimental results show that carbonate species formed on the surfaces is closely related to the oxidation process. Therefore, in this study, we considered the adsorbed carbonate species (E1 and E4) in the reaction mechanism.

As shown in Figure 3a, the first oxidation is initiated by CO adsorption onto RE-doped $CeO_2(111)$. The CO molecule adsorbs strongly at the bridge site between the two adjacent lattice oxygen atoms on the surface with the formation of carbonate species (E1). The molecule is then transformed to the adsorbed CO_2 (IS1), followed by desorption from the surface, leaving an oxygen vacancy (E2). Because the CO_2-like species adsorbed vertically on the surface exists as an intermediate step (IS1) from carbonate species to the gas phase CO_2, it is regarded as a metastable state for the CO_2 desorption. This is consistent with previous theoretical reports in that the vertically linear configuration of chemisorbed CO_2 is observed during the CO oxidation process on M-doped CeO_2 (M = Mn, Ru, and Fe).[40−42]

Although the first oxidation cycle does not restore RE-doped $CeO_{2-x}(111)$ to its initial state, the consecutive reactions of a second oxidation cycle recover the surfaces, making further continuous reactions possible. O_2 adsorption onto the oxygen vacancy site initiates a second oxidation process, with healing of the defected surfaces. After the adsorption of O_2, excess lattice oxygen remains on the surface (E3), where a CO molecule can bind easily. Upon the second CO adsorption, another carbonate species is formed on the surface (E4). The speices is then transformed to adsorbed CO_2 (IS2), which would be desorbed as CO_2 gas from the RE-doped $CeO_2(111)$, with a regeneration of the clean surface (E5).

From the reaction profile in Figure 3a, the key reaction barriers of CO oxidation are the endothermic elementary steps of the transformation from carbonate-like species to adsorbed CO_2 (E1 → IS1 and E4 → IS2) or CO_2 desorption (IS1 → E2 and IS2 → E5). Owing to the endothermicity, the four elementary steps (E1 → IS1, IS1 → E2, E4 → IS2, and IS2 →

DOI: 10.1021/acsami.7b01844
ACS Appl. Mater. Interfaces 2017, 9, 15449−15458

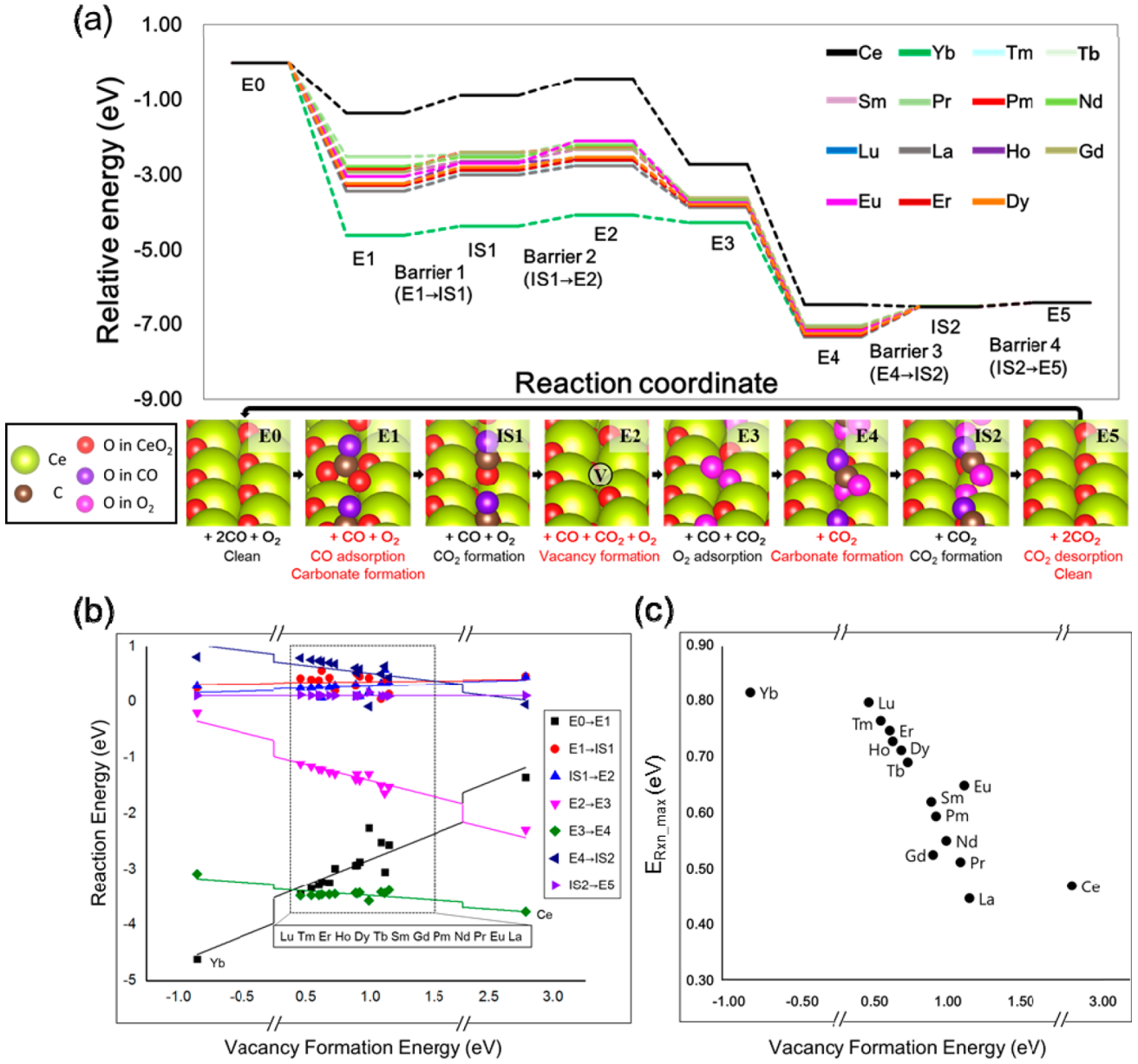

Figure 3. (a) Relative energy diagram of CO oxidation on RE-doped CeO_2(111). IS1 and IS2 represent the intermediate states of CO_2 desorption, respectively. The bottom insets in (a) represent the optimized structures of the oxidation process at each step on undoped CeO_2. The bottom two figures show a linear relationship between (b) the reaction energy of each elementary step or (c) E_{Rxn_max} and the formation energy of oxygen vacancy on RE-doped CeO_2(111).

E5) are denoted as barriers 1, 2, 3, and 4, respectively (Figure 3 and Table S1). To compare the activity of CO oxidation for each dopant, an elementary step with the highest reaction energy was selected among the four elementary steps (barriers 1−4), considering the step as an RDS. Table S1 lists the energetics of oxygen vacancy formation and the reaction barrier. All dopants, except for Ce, have the highest reaction energy (E_{Rxn_max}) at barrier 3, where the geometry of the adsorbate was changed from the carbonate-like to CO_2-like species (Figures 3 and S9), suggesting that barrier 3 is an RDS. A comparison of E_{Rxn_max} at the RDS on each RE-doped CeO_2(111) successfully explained the experimental results in that the activity of CO oxidation is in the order of CeO_2 > PDC > NDC > SDC. Therefore, investigating the elementary steps, including the carbonate species step through the MvK mechanism, is appropriate for predicting the dopant effect on the activity of CO oxidation on RE-doped CeO_2(111).

Similar to previous reports,[38,40−42] the reaction profile showed that the carbonate species as an adsorbate (E1 and E4) is more stable than the CO_2-like species (IS1 and IS2) at both the first and second oxidation processes, respectively. Although the optimized geometries are slightly different in terms of the tilt angles of the carbonate species formed on RE-doped CeO_2(111) depending on the dopants (Figure S6), doping RE-metals enhances the strength of molecular adsorption for all cases. Unlike the first intermediate species of CO_2 chemisorbed vertically at the surface (IS1) (−0.38 to −0.94 eV), the second intermediate species of CO_2 have weaker binding strengths (∼−0.12 eV), with adsorption configurations parallel to the surfaces for all dopants (IS2). This implies the independence of the adsorption strength on

DOI: 10.1021/acsami.7b01844
ACS Appl. Mater. Interfaces 2017, 9, 15449−15458

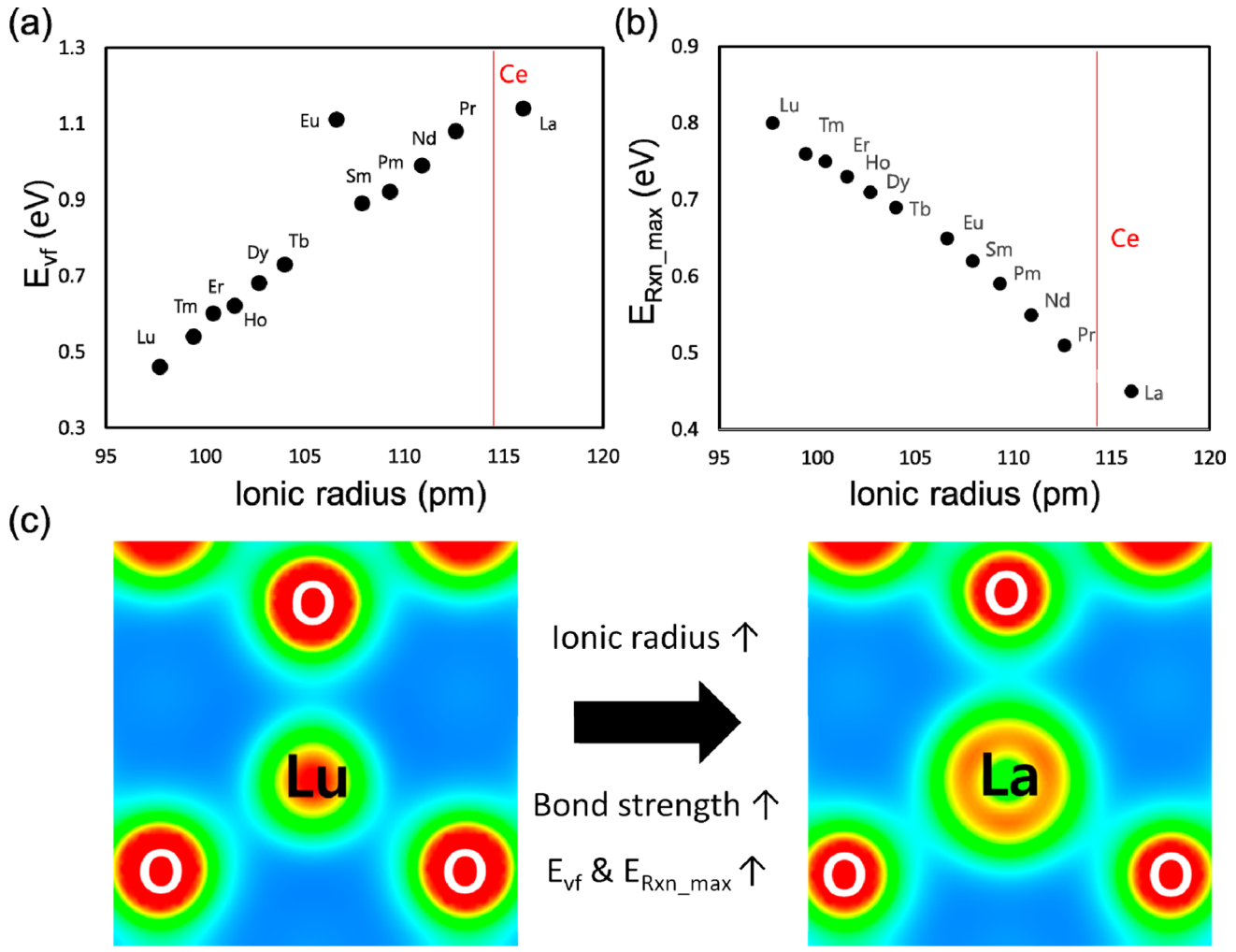

Figure 4. Linear relationships between (a) oxygen vacancy formation energies or (b) E_{Rxn_max} and the ionic radius of dopants on RE-doped CeO_2(111). (c) Charge density distribution of RE dopants with the smallest (Lu) and the largest (La) ionic radius bonded with the NN oxygen atoms in RE-doped CeO_2(111).

the types of dopants (Figure S6), which is evidence of physisorption.[62] The adsorption strength of CO_2 is sensitive to the defects on the surface because the main difference between IS1 and IS2 is the existence of oxygen vacancies near the adsorption site. This may be due to the accumulation of surface charge near the oxygen vacancy;[63] the formation of oxygen vacancies during the first oxidation process leaves excess charges on the surfaces, inducing a strong chemisorption of CO_2.[40−42] This is also supported by a previous report that CO_2 adsorption on O-defective CeO_2(111) is stronger than that on a clean surface.[50] Therefore, more energy is required to proceed from the carbonate species formed on the surface (E4 or E1) to the CO_2-physisorbed state (IS2) at barrier 3 than that required to proceed to the CO_2-chemisorbed state (IS1) at barrier 1. From these different reaction characteristics, barrier 3 is determined to be an RDS for the CO oxidation reaction on RE-doped CeO_2(111).

3.4. Linear Relationship between Oxygen Vacancy Formation and CO Oxidation Activity on RE-Doped CeO_2(111). In the MvK mechanism, the atomic oxygen supplied by the lattice oxygen of CeO_2 oxidizes the CO reactant. The capturing process of lattice oxygen to the CO molecule is accompanied by the formation of a surface oxygen vacancy (IS1 and E2) or the removal of excess oxygen (IS2 and E5). Therefore, the oxygen vacancy formation energy (E_{vf}), which is a measure of how easily oxygen vacancies are formed, is a key descriptive factor for analyzing the CO oxidation on doped CeO_2.[11,40−42,44,64] Aryanpour et al. previously explored the relationship between the oxygen vacancy formation energies from DFT calculations and the experimentally measured catalytic activity for various TM or noble metal-doped CeO_2 in several reactions, such as the preferential oxidation of CO (Fe and Zr-doped CeO_2), soot conversion (Cu, Fe, and Y doped CeO_2), and N_2O conversion (Rh, Pt, and Pd-doped CeO_2).[64] They reported that the oxygen vacancy formation energies on TM- or noble metal-doped CeO_2 are inversely proportional to the catalytic activities, suggesting that the easier formation of oxygen vacancies is closely related to the higher activity of surface reactions.

The relationships between E_{vf} and the reaction energies (linearly correlated with the reaction barriers via BEP, as described in Figure S5) for all elementary steps were also explored. Because all reaction energies in these results show linear relationships with E_{vf} (Figure 4a), oxygen vacancy formation is closely related to the activity of CO oxidation on RE-doped CeO_2(111). Unlike the cases of TM or noble metal-doped CeO_2, however, there was a linear (an inverse) relationship between E_{vf} and the activity (E_{Rxn_max}), indicating

DOI: 10.1021/acsami.7b01844
ACS Appl. Mater. Interfaces 2017, 9, 15449−15458

that the easier formation of oxygen vacancies deteriorates the activity of CO oxidation on RE-doped $CeO_2(111)$ (Figure 4b). To determine how this relationship is established, the RDS, that is, barrier 3 (E4 → IS2), was examined. In the second oxidation process, one O atom (O_{latt}) of the adsorbed oxygen molecule (E3) recovers the surface vacancy while the other O atom (O_c) binds to the adsorbing CO molecules by forming the surface carbonate (E4) (Figure S7). At barrier 3, the carbonate species transforms to physisorbed CO_2, leaving a clean surface. This process can be much easier if O_{latt} binds weakly to the CO_2 part of the carbonate species, which will be desorbed as gas phase CO_2 via the CO_2-physisorbed state (IS2). The weaker binding of O_{latt} to CO_2 is, in turn, connected directly to the stronger bonding of O_{latt} to the surface cations. The bond length between the C atom and O_{latt} atom in the carbonate species (d_{C-O}) (Figure S7a) and the average bond lengths between O_{latt} and three nearest neighbor (NN) cations on the carbonate-formed surface relative to those on the clean surface ($d_{cation-O}$) were measured (Figure S7b). As shown in Figure S7, the results show that d_{C-O} ($d_{cation-O}$) is (inversely) proportional to E_{vf}. This suggests that higher E_{vf} indicates the higher affinity of lattice oxygen to the cations (contracted $d_{cation-O}$) in $CeO_2(111)$, leading to stretched d_{C-O}. Therefore, a higher E_{vf} accelerates the easier transformation of the carbonate species to the physisorbed CO_2 due to the weaker binding of O_{latt} to CO_2, which lowers the energy barrier in an RDS. E_{vf} has a linear (an inverse) relationship to activity (E_{Rxn_max}) because all RE-doped CeO_2 have RDS at barrier 3.

3.5. Simple Descriptor to Predict the Activity of CO Oxidation Reaction on RE-Doped $CeO_2(111)$. Doping CeO_2 with RE metals with different ionic radii (R_{ion}) results in different structural and chemical properties compared to those of CeO_2. Although there have been several studies that showed the relationship between R_{ion} and various properties of RE-doped CeO_2, such as oxygen migration, oxygen vacancy formation, and catalytic activity,[65] most studies were conducted on bulk ceria.

Recently, Ke et al. examined the activity of CO oxidation on RE-doped CeO_2 (RE = La−Lu) nanowires.[66] Except for La-, Pr-doped, and pure CeO_2, their experimental results also showed a linear relationship between R_{ion} and the catalytic activity. Unlike this study, however, their results had some limitations. The catalysts they prepared showed a relatively wide distribution of particle sizes, compositions, and surface areas, which is difficult to compare entirely with the theoretical results. In addition, they did not explore thoroughly the overall mechanism of the oxidation reaction for all lanthanide dopants by theoretical analysis. Indeed, here we demonstrated that the catalytic activities on La-, Pr-doped, and pure CeO_2 that did not show a linear trend from Ke et al.'s results also showed a linear relationship with R_{ion}. Therefore, it might be difficult for them to elucidate the factors governing the activity of CO oxidation even though they tried to examine the relationship between E_{vf} or R_{ion} and the catalytic activity on RE-doped CeO_2.

In this study, we precisely examined the overall surface reaction of CO oxidation on RE-doped $CeO_2(111)$, where all molecular reactions occur next to the dopants (Figure S6). In Figure 3, E_{vf} can act as a descriptor to predict the catalytic activity of CO oxidation as reported elsewhere.[40−42,50] Because E_{vf} is governed by the interaction between the cation and oxygen ion, it is necessary to explore the interactions between RE and lattice oxygen to determine the origin of different E_{vf} over various RE-doped CeO_2. Andersson et al. reported a linear relationship between the atomic number and E_{vf} in RE-doped bulk ceria by performing DFT calculations.[67] To investigate the contribution of the dopant to the formation of oxygen vacancies, they divided the vacancy−dopant interactions into elastic and electronic parts. Although both contributions are directly/inversely proportional to the atomic number of the RE metal dopants, overall, the elastic interaction energy describes well the general trend of the total dopant−oxygen interaction energy, when oxygen vacancies are formed at the nearest neighbor of the dopant. In addition, RE dopants are in a constant charge state, which is in contrast to TM or noble metal dopants, indicating that the electronic contribution of RE dopants is not critical. Gupta et al. investigated OSC in TM (Mn, Fe, Co, Ni, and Cu), noble metal (Pd, Pt, and Ru), and RE metal (Y and La)-doped CeO_2. They found from both experiments and DFT calculations that after reduction, the TMs altered the charge state from 3+ to 2+ and noble metals often changed from 2+ to 0 while RE metals still held 3+ charge states. Therefore, it is expected that the elastic property is related much more closely to the activity of CO oxidation than to the electronic one.[68]

To carefully examine the elastic contribution from the different sizes of dopant (R_{ion}) to the RE−O interaction that would be associated directly with E_{vf} (Table S2),[25,69] the RE−O bond strengths were calculated as the charge density distribution between RE and O. Note that Ce^{4+} satisfies the charge stoichiometry of pure CeO_2, but for defective CeO_2, Ce often has facile changeability between Ce^{4+}/Ce^{3+}. The charge state of Ce on pure $CeO_2(111)$ can thus be 3+, which has an ionic radius of 114.3 pm, while other RE metals that have 3+ charge states in CeO_2 have relatively smaller ionic radii than Ce^{3+} except for La. Therefore, structural stress, such as microtensile strain, is induced between RE and O. Figure 4c shows that the microstrain induced by the smaller dopant size weakens the cation−oxygen bond strength.[69,70] For this reason, dopants with a lower ionic radius result in a lower E_{vf} (Figure 4a), demonstrating that R_{ion} is closely related to E_{vf}.

Summarizing all relationships of the terms discussed so far (R_{ion}, E_{vf}, E_{Rxn}, and E_b), a series of linear relationships was found between $R_{ion} \propto E_{vf} \propto E_{Rxn} \propto E_b$. Therefore, the catalytic activity of CO oxidation on RE-doped $CeO_2(111)$ can be predicted by simply using R_{ion}, as shown in Figure 4b. In Figure 3c, however, there were some discrepancies for the linear relationships on Yb- or Gd-doped $CeO_2(111)$, which might be due to the relatively strong magnetic properties. Previous experiments showed that Gd-doped CeO_2 has much weaker magnetic properties than pure CeO_2.[71] Therefore, Aparicio-Anglès previously performed DFT calculations by artificially treating the spin state as null to explore the mobility of oxygen vacancies on Gd-doped $CeO_2(111)$.[72] On the other hand, the current spin-polarized DFT calculations for Yb- and Gd-doped $CeO_2(111)$ obtained a more stable energy state at a higher spin state than in the case of null total spin, which may result in unique characteristics due to doping RE^{3+} ions with the stronger magnetic properties.[71] For this reason, the data points for Yb- and Gd-doped $CeO_2(111)$ in Figure 4 were excluded to emphasize the general relationship between the ionic radius of the RE dopant and the catalytic activity of RE-doped $CeO_2(111)$.

In contrast to RE-doped CeO_2, many studies of TM-doped CeO_2 reported that a lower E_{vf} indicates higher catalytic activity. Until now, there has been a lack of comprehensive research for a mechanistic study of CO oxidation through a

DOI: 10.1021/acsami.7b01844
ACS Appl. Mater. Interfaces 2017, 9, 15449−15458

wide range of TM-doped CeO_2(111). Therefore, it is difficult to identify precisely why an opposite relationship between E_{vf} and the catalytic activity of CO oxidation was observed. For TM-doped CeO_2, there might be complicated reasons for the general trend, such as charge changeability and the ionic size of the dopant, charge transfer between the adsorbate and catalyst, and catalyst morphology. Among them, the difference in the position of the RDS and the distinct elastic/electronic characteristics of the dopant elements between RE- and TM-doped CeO_2(111) may provide some clue to the different dependence of the catalytic activity on E_{vf}. For example, Chen et al. performed DFT calculations to examine the CO oxidation on Fe-doped CeO_2, showing that a phase transition step from carbonate (CO_3^{2-}) species to CO_2-like species in the first oxidation process is the RDS of CO oxidation on Fe-doped CeO_2(111).[40] Our previous result also showed that Fe-doped CeO_2(111) has the RDS at the first oxidation process (E1 → IS1).[73] In addition, the oxidation state of the TM dopants in TM-doped CeO_2 can be changed from 3+ to 2+.[68] Because a higher oxidation state often leads to a smaller ionic radius, such charge changeability makes it much more complicated to identify the fundamental reason for the overall relationship between E_{vf} and the catalytic activity on TM-doped CeO_2(111) than that on the RE-doped one. To clearly distinguish the dependence of the catalytic activity on E_{vf} between TM and RE dopants, more detailed studies of various TM-doped CeO_2 are required.

In summary, R_{ion} can act as a simple descriptor to rapidly predict the activity of CO oxidation on RE-doped CeO_2. On the basis of these results, Figure 4b suggests that among the RE-doped CeO_2, La-doped CeO_2 may be promising for CO oxidation. Experimental verification of the CO oxidation activity on La-doped CeO_2 is currently underway.

4. CONCLUSIONS

In this study, the effects of dopants on the catalytic properties of CeO_2 were analyzed precisely by examining the activities of CO oxidation on CeO_2, PDC, NDC, and SDC NPs with well controlled morphologies and compositions. The experimental results showed that the catalytic activities of doped ceria NPs were in the order of CeO_2 > PDC > NDC > SDC. In addition, the reaction mechanism of CO oxidation on RE-doped CeO_2(111) was investigated using first-principles calculations via the MvK mechanism.

On the basis of a careful mechanistic study, a strong linear relationship was found between R_{ion} and the catalytic activity represented by E_{Rxn_max} at a RDS, which was derived as follows:

(1) Microstrain from localized lattice expansion or contraction induced by doping the different size (R_{ion}) of RE metals alters the E_{vf}.
(2) Because E_{Rxn_max} of CO oxidation has a linear relationship with E_{vf}, it can also be estimated by R_{ion} of RE metals.
(3) Consequently, R_{ion} can act as a simple descriptor to predict the activity of CO oxidation on RE-doped CeO_2(111).

From these results, La-doped CeO_2 is a promising catalyst for CO oxidation among RE-doped CeO_2, which will be validated in a future study. These results will play an important role in elucidating the effects of dopants on the catalytic activity of ceria and developing high performance CeO_2-based catalysts.

ASSOCIATED CONTENT

Supporting Information

The Supporting Information is available free of charge on the ACS Publications website at DOI: 10.1021/acsami.7b01844.

Additional data, figures, and tables with descriptions (PDF)

AUTHOR INFORMATION

Corresponding Authors

*E-mail: wcjung@kaist.ac.kr (W.J.).
*E-mail: jwhan@uos.ac.kr (J.W.H.).

ORCID

Kyeounghak Kim: 0000-0003-1297-6038
Minseok Bae: 0000-0003-0293-5355
Joongmyeon Bae: 0000-0001-9719-1779
Jeong Woo Han: 0000-0001-5676-5844

Author Contributions

‖K.K. and J.Y. contributed equally to this work.

Notes

The authors declare no competing financial interest.

ACKNOWLEDGMENTS

The authors acknowledge support from the National Research Foundation of Korea (NRF) grant funded by the Korea government (MSIP) (NRF-2014M3A6A7074784, NRF-2011-0031569, and NRF-2016R1A5A1009592).

REFERENCES

(1) Cargnello, M.; Doan-Nguyen, V. V. T.; Gordon, T. R.; Diaz, R. E.; Stach, E. A.; Gorte, R. J.; Fornasiero, P.; Murray, C. B. Control of Metal Nanocrystal Size Reveals Metal-Support Interface Role for Ceria Catalysts. *Science* **2013**, *341*, 771−773.
(2) Sun, C.; Li, H.; Chen, L. Nanostructured Ceria-Based Materials: Synthesis, Properties, and Applications. *Energy Environ. Sci.* **2012**, *5*, 8475−8505.
(3) Jung, W.; Dereux, J. O.; Chueh, W. C.; Hao, Y.; Haile, S. M. High Electrode Activity of Nanostructured, Columnar Ceria Films for Solid Oxide Fuel Cells. *Energy Environ. Sci.* **2012**, *5*, 8682−8689.
(4) Chueh, W. C.; Hao, Y.; Jung, W.; Haile, S. M. High Electrochemical Activity of the Oxide Phase in Model Ceria−Pt and Ceria−Ni Composite Anodes. *Nat. Mater.* **2012**, *11*, 155−161.
(5) Rodriguez, J. A.; Ma, S.; Liu, P.; Hrbek, J.; Evans, J.; Pérez, M. Activity of CeO_x and TiO_x Nanoparticles Grown on Au(111) in the Water-Gas Shift Reaction. *Science* **2007**, *318*, 1757−1760.
(6) O'Connell, M.; Morris, M. A. New Ceria-Based Catalysts for Pollution Abatement. *Catal. Today* **2000**, *59*, 387−393.
(7) Trovarelli, A.; de Leitenburg, C.; Boaro, M.; Dolcetti, G. The Utilization of Ceria in Industrial Catalysis. *Catal. Today* **1999**, *50*, 353−367.
(8) Kašpar, J.; Fornasiero, P. Nanostructured Materials for Advanced Automotive De-Pollution Catalysts. *J. Solid State Chem.* **1999**, *50*, 285−298.
(9) Trovarelli, A. Catalytic Properties of Ceria and CeO_2-Containing Materials. *Catal. Rev.* **1996**, *38*, 439−520.
(10) Carrettin, S.; Concepción, P.; Corma, A.; López Nieto, J. M.; Puntes, V. F. Nanocrystalline CeO_2 Increases the Activity of Au for CO Oxidation by Two Orders of Magnitude. *Angew. Chem., Int. Ed.* **2004**, *43*, 2538−2540.
(11) Wu, Z.; Li, M.; Overbury, S. H. On the Structure Dependence of CO Oxidation over CeO_2 Nanocrystals with Well-Defined Surface Planes. *J. Catal.* **2012**, *285*, 61−73.
(12) Xiao, G.; Li, S.; Li, H.; Chen, L. Synthesis of Doped Ceria with Mesoporous Flowerlike Morphology and Its Catalytic Performance for CO Oxidation. *Microporous Mesoporous Mater.* **2009**, *120*, 426−431.

DOI: 10.1021/acsami.7b01844
ACS Appl. Mater. Interfaces 2017, 9, 15449−15458

(13) Zhou, H.-P.; Zhang, Y.-W.; Si, R.; Zhang, L.-S.; Song, W.-G.; Yan, C.-H. Dimension-Manipulated Ceria Nanostructures (0D Uniform Nanocrystals, 2D Polycrystalline Assembly, and 3D Mesoporous Framework) from Cerium Octylate Precursor in Solution Phases and Their CO Oxidation Activities. *J. Phys. Chem. C* **2008**, *112*, 20366−20374.
(14) Zhang, J.; Kumagai, H.; Yamamura, K.; Ohara, S.; Takami, S.; Morikawa, A.; Shinjoh, H.; Kaneko, K.; Adschiri, T.; Suda, A. Extra-Low-Temperature Oxygen Storage Capacity of CeO_2 Nanocrystals with Cubic Facets. *Nano Lett.* **2011**, *11*, 361−364.
(15) Rao, R.; Yang, M.; Li, C.; Dong, H.; Fang, S.; Zhang, A. A Facile Synthesis for Hierarchical Porous CeO_2 Nanobundles and Their Superior Catalytic Performance for CO Oxidation. *J. Mater. Chem. A* **2015**, *3*, 782−788.
(16) Zhang, D.; Pan, C.; Shi, L.; Huang, L.; Fang, J.; Fu, H. A Highly Reactive Catalyst for CO Oxidation: CeO_2 Nanotubes Synthesized using Carbon Nanotubes as Removable Templates. *Microporous Mesoporous Mater.* **2009**, *117*, 193−200.
(17) Park, Y.; Kim, S. K.; Pradhan, D.; Sohn, Y. Surface Treatment Effects on CO Oxidation Reactions over Co, Cu, and Ni-Doped and codoped CeO_2 Catalysts. *Chem. Eng. J.* **2014**, *250*, 25−34.
(18) Elias, J. S.; Risch, M.; Giordano, L.; Mansour, A. N.; Shao-Horn, Y. Structure, Bonding, and Catalytic Activity of Monodisperse, Transition-Metal-Substituted CeO_2 Nanoparticles. *J. Am. Chem. Soc.* **2014**, *136*, 17193−17200.
(19) Ranløv, J.; Poulsen, F. W.; Mogensen, M. Comment on "The Characterization of Doped CeO_2 Electrodes in Solid Oxide Fuel Cells" by B.G. Pound, Solid State Ionics 52 (1992) 183−188. *Solid State Ionics* **1993**, *61*, 277−279.
(20) Tianshu, Z.; Hing, P.; Huang, H.; Kilner, J. The Effect of Fe Doping on the Sintering Behavior of Commercial CeO_2 Powder. *J. Mater. Process. Technol.* **2001**, *113*, 463−468.
(21) Balakirev, V. F.; Golikov, Y. V. Heterogeneous Phase Equilibria in Rare Earth−Mn−O Systems in Air. *Inorg. Mater.* **2003**, *39*, S1−S10.
(22) Ivas, T.; Grundy, A. N.; Povoden-Karadeniz, E.; Gauckler, L. J. Phase Diagram of CeO_2−CoO for Nano-Sized Powders. *Calphad* **2012**, *36*, 57−64.
(23) Inaba, H.; Tagawa, H. Ceria-Based Solid Electrolytes. *Solid State Ionics* **1996**, *83*, 1−16.
(24) Mogensen, M.; Sammes, N. M.; Tompsett, G. A. Physical, Chemical and Electrochemical Properties of Pure and Doped Ceria. *Solid State Ionics* **2000**, *129*, 63−94.
(25) Rupp, J. L. M.; Fabbri, E.; Marrocchelli, D.; Han, J.-W.; Chen, D.; Traversa, E.; Tuller, H. L.; Yildiz, B. Scalable Oxygen-Ion Transport Kinetics in Metal-Oxide Films: Impact of Thermally Induced Lattice Compaction in Acceptor Doped Ceria Films. *Adv. Funct. Mater.* **2014**, *24*, 1562−1574.
(26) Aneggi, E.; Boaro, M.; Leitenburg, C. d.; Dolcetti, G.; Trovarelli, A. Insights into the Redox Properties of Ceria-Based Oxides and Their Implications in Catalysis. *J. Alloys Compd.* **2006**, *408*−*412*, 1096−1102.
(27) Reddy, B. M.; Katta, L.; Thrimurthulu, G. Novel Nanocrystalline $C_{e1-x}La_xO_{2-\delta}$ (x = 0.2) Solid Solutions: Structural Characteristics and Catalytic Performance. *Chem. Mater.* **2010**, *22*, 467−475.
(28) Reddy, B.; Thrimurthulu, G.; Katta, L. Design of Efficient $Ce_xM_{1-x}O_{2-\delta}$ (M = Zr, Hf, Tb and Pr) Nanosized Model Solid Solutions for CO Oxidation. *Catal. Lett.* **2011**, *141*, 572−581.
(29) Durgasri, D. N.; Vinodkumar, T.; Sudarsanam, P.; Reddy, B. Nanosized CeO_2−Gd_2O_3 Mixed Oxides: Study of Structural Characterization and Catalytic CO Oxidation Activity. *Catal. Lett.* **2014**, *144*, 971−979.
(30) Vinodkumar, T.; Rao, B. G.; Reddy, B. M. Influence of Isovalent and Aliovalent Dopants on the Reactivity of Cerium Oxide for Catalytic Applications. *Catal. Today* **2015**, *253*, 57−64.
(31) Prasad, D. H.; Park, S. Y.; Ji, H. I.; Kim, H. R.; Son, J. W.; Kim, B. K.; Lee, H. W.; Lee, J. H. Structural Characterization and Catalytic Activity of $Ce_{0.65}Zr_{0.25}RE_{0.1}O_{2-\delta}$ Nanocrystalline Powders Synthesized by the Glycine-Nitrate Process. *J. Phys. Chem. C* **2012**, *116*, 3467−3476.
(32) Harshini, D.; Lee, D. H.; Jeong, J.; Kim, Y.; Nam, S. W.; Ham, H. C.; Han, J. H.; Lim, T.-H.; Yoon, C. W. Enhanced Oxygen Storage Capacity of $Ce_{0.65}Hf_{0.25}M_{0.1}O_{2-\delta}$ (M = Rare Earth Elements): Applications to Methane Steam Reforming with High Coking Resistance. *Appl. Catal., B* **2014**, *148*−*149*, 415−423.
(33) Zhao, S.; Gorte, R. J. The Effect of Oxide Dopants in Ceria on n-Butane Oxidation. *Appl. Catal., A* **2003**, *248*, 9−18.
(34) Zhao, S.; Gorte, R. J. A Comparison of Ceria and Sm-Doped Ceria for Hydrocarbon Oxidation Reactions. *Appl. Catal., A* **2004**, *277*, 129−136.
(35) Song, W.; Jansen, A. P. J.; Hensen, E. J. M. A Computational Study of the Influence of the Ceria Surface Termination on the Mechanism of CO Oxidation of Isolated Rh Atoms. *Faraday Discuss.* **2013**, *162*, 281−292.
(36) Nolan, M.; Grigoleit, S.; Sayle, D. C.; Parker, S. C.; Watson, G. W. Density Functional Theory Studies of the Structure and Electronic Structure of Pure and Defective Low Index Surfaces of Ceria. *Surf. Sci.* **2005**, *576*, 217−229.
(37) Kim, H. Y.; Henkelman, G. CO Oxidation at the Interface between Doped CeO_2 and Supported Au Nanoclusters. *J. Phys. Chem. Lett.* **2012**, *3*, 2194−2199.
(38) Chen, F.; Liu, D.; Zhang, J.; Hu, P.; Gong, X.-Q.; Lu, G. A DFT + U study of the Lattice Oxygen Reactivity Toward Direct CO Oxidation on the CeO_2(111) and (110) Surfaces. *Phys. Chem. Chem. Phys.* **2012**, *14*, 16573−16580.
(39) Migani, A.; Vayssilov, G. N.; Bromley, S. T.; Illas, F.; Neyman, K. M. Dramatic Reduction of the Oxygen Vacancy Formation Energy in Ceria Particles: A Possible Key to Their Remarkable Reactivity at the Nanoscale. *J. Mater. Chem.* **2010**, *20*, 10535−10546.
(40) Chen, H.-T.; Chang, J.-G. Computational Investigation of CO Adsorption and Oxidation on Iron-Modified Cerium Oxide. *J. Phys. Chem. C* **2011**, *115*, 14745−14753.
(41) Chen, H.-T. First-Principles Study of CO Adsorption and Oxidation on Ru-Doped CeO_2(111) Surface. *J. Phys. Chem. C* **2012**, *116*, 6239−6246.
(42) Hsu, L.-C.; Tsai, M.-K.; Lu, Y.-H.; Chen, H.-T. Computational Investigation of CO Adsorption and Oxidation on Mn/CeO_2(111) Surface. *J. Phys. Chem. C* **2013**, *117*, 433−441.
(43) Song, W.; Su, Y.; Hensen, E. J. M. A DFT Study of CO Oxidation at the Pd−CeO_2(110) Interface. *J. Phys. Chem. C* **2015**, *119*, 27505−27511.
(44) Yang, Z.; Wei, Y.; Fu, Z.; Lu, Z.; Hermansson, K. Facilitated Vacancy Formation at Zr-doped Ceria(111) Surfaces. *Surf. Sci.* **2008**, *602*, 1199−1206.
(45) Kim, H. Y.; Lee, H. M.; Henkelman, G. CO Oxidation Mechanism on CeO_2-Supported Au Nanoparticles. *J. Am. Chem. Soc.* **2012**, *134*, 1560−1570.
(46) Shao, Z.; Yang, W.; Cong, Y.; Dong, H.; Tong, J.; Xiong, G. Investigation of the Permeation Behavior and Stability of a $Ba_{0.5}Sr_{0.5}Co_{0.8}Fe_{0.2}O_{3-\delta}$ Oxygen Membrane. *J. Membr. Sci.* **2000**, *172*, 177−188.
(47) Kresse, G.; Furthmüller, J. Efficient Iterative Schemes for ab initio Total-Energy Calculations using a Plane-Wave Basis Set. *Phys. Rev. B: Condens. Matter Mater. Phys.* **1996**, *54*, 11169−11186.
(48) Sholl, D. S.; Steckel, J. A. Index. In *Density Functional Theory*; John Wiley & Sons, Inc., 2009; pp 235−238.
(49) Yang, Z.; Woo, T. K.; Baudin, M.; Hermansson, K. Atomic and Electronic Structure of Unreduced and Reduced CeO_2 Surfaces: A First-Principles Study. *J. Chem. Phys.* **2004**, *120*, 7741−7749.
(50) Conesa, J. Computer Modeling of Surfaces and Defects on Cerium Dioxide. *Surf. Sci.* **1995**, *339*, 337−352.
(51) Aneggi, E.; Llorca, J.; Boaro, M.; Trovarelli, A. Surface-Structure Sensitivity of CO Oxidation over Polycrystalline Ceria Powders. *J. Catal.* **2005**, *234*, 88−95.
(52) Yang, C.; Yu, X.; Heißler, S.; Nefedov, A.; Colussi, S.; Llorca, J.; Trovarelli, A.; Wang, Y.; Wöll, C. Surface Faceting and Reconstruction of Ceria Nanoparticles. *Angew. Chem., Int. Ed.* **2017**, *56*, 375−379.
(53) Perdew, J. P.; Burke, K.; Ernzerhof, M. Generalized Gradient Approximation Made Simple. *Phys. Rev. Lett.* **1996**, *77*, 3865−3868.

DOI: 10.1021/acsami.7b01844
ACS Appl. Mater. Interfaces 2017, 9, 15449−15458

(54) Monkhorst, H. J.; Pack, J. D. Special Points for Brillouin-Zone Integrations. *Phys. Rev. B* **1976**, *13*, 5188−5192.
(55) Tan, J. P. Y.; Tan, H. R.; Boothroyd, C.; Foo, Y. L.; He, C. B.; Lin, M. Three-Dimensional Structure of CeO_2 Nanocrystals. *J. Phys. Chem. C* **2011**, *115*, 3544−3551.
(56) Maya-Johnson, S.; Gracia, L.; Longo, E.; Andres, J.; Leite, E. R. Synthesis of Cuboctahedral CeO_2 Nanoclusters and Their Assembly into Cuboid Nanoparticles by Oriented Attachment. *ChemNanoMat* **2017**, 228−232.
(57) Zhou, K.; Wang, X.; Sun, X.; Peng, Q.; Li, Y. Enhanced Catalytic Activity of Ceria Nanorods from Well-Defined Reactive Crystal Planes. *J. Catal.* **2005**, *229*, 206−212.
(58) Capdevila-Cortada, M.; López, N. Descriptor Analysis in Methanol Conversion on Doped CeO_2(111): Guidelines for Selectivity Tuning. *ACS Catal.* **2015**, *5*, 6473−6480.
(59) Henkelman, G.; Uberuaga, B. P.; Jónsson, H. A Climbing Image Nudged Elastic Band Method for Finding Saddle Points and Minimum Energy Paths. *J. Chem. Phys.* **2000**, *113*, 9901−9904.
(60) Lu, X.; Wang, W.; Wei, S.; Guo, C.; Shao, Y.; Zhang, M.; Deng, Z.; Zhu, H.; Guo, W. Initial Reduction of CO_2 on Perfect and O-Defective CeO_2 (111) Surfaces: Towards CO or COOH? *RSC Adv.* **2015**, *5*, 97528−97535.
(61) Xie, T.; Wang, X.-D.; Yao, M.; Liu, X.-S.; Chen, Y.-G. First-Principle Study of CO Adsorption and Oxidation on Sm-Doped CeO_2(111) Surface. *RSC Adv.* **2016**, *6*, 20349−20356.
(62) Ko, J.; Kim, B.-K.; Han, J. W. Density Functional Theory Study for Catalytic Activation and Dissociation of CO_2 on Bimetallic Alloy Surfaces. *J. Phys. Chem. C* **2016**, *120*, 3438−3447.
(63) Kim, K.; Lee, W.; Han, J. W. First-Principles Study of Enhanced Oxygen Incorporation near the Grain Boundary on Yttria-Stabilized Zirconia. *Sci. Adv. Mater.* **2016**, *8*, 196−200.
(64) Aryanpour, M.; Khetan, A.; Pitsch, H. Activity Descriptor for Catalytic Reactions on Doped Cerium Oxide. *ACS Catal.* **2013**, *3*, 1253−1262.
(65) Alaydrus, M.; Sakaue, M.; Kasai, H. A DFT + U Study on the Contribution of 4f Electrons to Oxygen Vacancy Formation and Migration in Ln-doped CeO_2. *Phys. Chem. Chem. Phys.* **2016**, *18*, 12938−12946.
(66) Ke, J.; Xiao, J.-W.; Zhu, W.; Liu, H.; Si, R.; Zhang, Y.-W.; Yan, C.-H. Dopant-Induced Modification of Active Site Structure and Surface Bonding Mode for High-Performance Nanocatalysts: CO Oxidation on Capping-free (110)-oriented CeO_2:Ln (Ln = La−Lu) Nanowires. *J. Am. Chem. Soc.* **2013**, *135*, 15191−15200.
(67) Andersson, D. A.; Simak, S. I.; Skorodumova, N. V.; Abrikosov, I. A.; Johansson, B. Optimization of Ionic Conductivity in Doped Ceria. *Proc Natl Acad Sci U.S.A.* **2006**, *103*, 3518−3521.
(68) Gupta, A.; Waghmare, U.; Hegde, M. Correlation of Oxygen Storage Capacity and Structural Distortion in Transition-Metal-, Noble-Metal-, and Rare-Earth-Ion-Substituted CeO_2 from First Principles Calculation. *Chem. Mater.* **2010**, *22*, 5184−5198.
(69) Ma, D.; Lu, Z.; Tang, Y.; Li, T.; Tang, Z.; Yang, Z. Effect of Lattice Strain on the Oxygen Vacancy Formation and Hydrogen Adsorption at CeO_2(111) surface. *Phys. Lett. A* **2014**, *378*, 2570−2575.
(70) Rushton, M. J. D.; Chroneos, A. Impact of Uniaxial Strain and Doping on Oxygen Diffusion in CeO_2. *Sci. Rep.* **2014**, *4*, No. 6068.
(71) Li, G.-R.; Qu, D.-L.; Arurault, L.; Tong, Y.-X. Hierarchically Porous Gd^{3+}-doped CeO_2 Nanostructures for the Remarkable Enhancement of Optical and Magnetic Properties. *J. Phys. Chem. C* **2009**, *113*, 1235−1241.
(72) Aparicio-Anglès, X.; Roldan, A.; de Leeuw, N. H. Gadolinium-Vacancy Clusters in the (111) Surface of Gadolinium-Doped Ceria: A Density Functional Theory Study. *Chem. Mater.* **2015**, *27*, 7910−7917.
(73) Kim, K.; Han, J. W. Mechanistic Study for Enhanced CO Oxidation Activity on (Mn,Fe) co-doped CeO_2(111) *Catal. Today* 2017. 10.1016/j.cattod.2016.11.046.

DOI: 10.1021/acsami.7b01844
ACS Appl. Mater. Interfaces 2017, 9, 15449−15458